Evaluation of Shock Standoff Distance using in-situ data and understanding the correlation with shock parameters and with the magnitude of SSCs

submitted by

Abhilash Biswas
(PHYS179)

DEPARTMENT OF PHYSICS
PONDICHERRY UNIVERSITY
605014, Puducherry, India

Under the guidance of

Dr. Wageesh Mishra

ASSOCIATE PROFESSOR
Indian Institute of Astrophysics
560034, Kormangala Block 2, Bengaluru,
India

Abstract

This project aims to build a foundational understanding of Coronal Mass Ejections (CMEs), beginning with their formation in the solar corona and their detection through remote sensing observations. The study follows the evolution of CMEs as they propagate through interplanetary space, where they are observed as Interplanetary CMEs (ICMEs) by spacecraft at L1 or other vantage points. Particular emphasis is placed on identifying key features in in-situ data, including shock arrival, sheath regions, and magnetic structures. The project investigates how various CME and shock-related parameters—such as standoff distance, shock speed, and compression ratio—are manifested in these observations and whether they correlate with geomagnetic storm strength, measured by indices like Dst. Through this analysis, the work explores potential relationships between interplanetary shock characteristics and their geoeffectiveness. While the conclusions are limited by a small sample size and data gaps.

Contents

1   Introduction

Coronal Mass Ejections (CMEs) are one of the important dynamic events taking place in the Sun, which have large influence not only in interplanetary space but also in near-Earth atmosphere, with the potential to cause instabilities in the space environment and damage space-borne instruments essential for communication and scientific interest, radiation impacts to cosmonauts, as well as affecting our atmosphere and life on Earth. Understanding the origin and dynamics of such dynamic and transient events is crucial for predicting these events, with preparedness that will help mitigate any large-scale instabilities. Since the 1980s, remote sensing scientific research has been conducted to understand the dynamics of the Sun as a whole. Recently, in situ studies have been performed to understand the impact of such transient events at near-Earth 1 AU (from the Sun) at near L1 by WIND, ACE, etc., to understand the impact of such plasma in the geomagnetic field of Earth, which is a long-standing problem [4]. Interplanetary space, as we
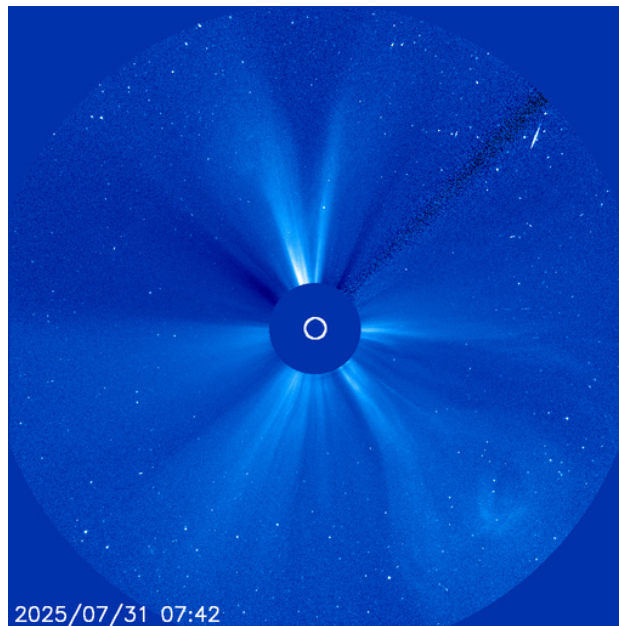

Fig 2: Solar corona observed via coronagraph using LASCO/C3 instrument, showing typical coronal structures [5].

know, is not static or empty. It is filled with dust, plasma, and energetic particles, which also have a large influence on the weather of Earth (which itself is a different area of study). Thus, understanding the kinematics of CMEs will also include their interaction with interplanetary space. Solar wind from the Sun consists of energetic particles, which are continuously showered on Earth, one effect of which is visible on Earth as Aurora Borealis in the Arctic poles, resulting from the interaction of these particles with our atmosphere. This is definitely influenced by Earth's magnetic field, which diverts such

particles. Understanding the interaction of solar wind and other transient events such as CMEs has great importance; different structures have been identified to be generated due to these interactions. Shock formation near Earth (bow shock) as well as shocks generated when high-speed streamers or CMEs move through relatively slow solar wind create another kind of shock; these shocks can cause instabilities in the space near Earth. Hence, understanding the parameters influencing the generation of such discontinuities is important. Studies conducted by different spacecraft at L1 have provided us with a better understanding of the local parameters of the space. LASCO, HI, and other instruments have provided us with white-light data that encompasses the field of view from the solar surface to 1 AU, giving us the opportunity to study these interactions. In this report, we will focus on understanding shock formation, how parameters such as density, speed, and magnetic field of CMEs and background wind dictate these structures in their evolution, and efforts to correlate shock standoff distances with geomagnetic activity.

1.1 The Solar Corona

The Solar Corona is a very hot, tenuous plasma region, which is much less dense than the photosphere but with a very high temperature of 6.0 (log scale), which itself is a long-standing question of how it is so hot compared to the photosphere (5678 K) or chromosphere (1000-10000 K). It consists of highly ionized plasma (Fe IV, Mg VI, etc.) and dust of low density. The Sun's emission peaks in the visible spectrum emitted by the abundant plasma in the photosphere, because of which it is not possible to observe the corona directly (emission peaks in the X-ray range). However, during a solar eclipse, when the Sun's photosphere is eclipsed by the Moon, the corona is visible. This light that we observe is the dust-scattered light from the photosphere. Hence, this is not the emission that we are seeing here; rather, we are seeing the F-corona, which is possible by the phenomenon known as Thomson Scattering (we will look more into this later). An eclipse, usually if it is a total solar eclipse, doesn't last longer than 7-8 minutes. To overcome this problem and enable continuous observation of the Sun, we can use a coronagraph, which is a device used to occult the photospheric disk. All heliospheric imaging techniques are possible using this coronagraph.

1.2 Data Collection

The study of CMEs and their associated shocks relies on two primary types of observational data: remote sensing and in-situ measurements. These com-

plementary approaches provide a comprehensive understanding of CME dynamics, from their initiation in the solar corona to their impact at 1 AU.

1.2.1 Remote Sensing Observations

Remote sensing data collection uses coronagraphs that occult the photospheric disk, examples of which are COR1-2/STEREO A/B or C1/LASCO. The scattered white light is captured, providing information on whether any transient events are taking place in the corona, which could be tracked to very high distances depending on the field of view of the coronagraph, typically to more than 30 solar radii. However, as these structures are 3D and our observation is based on projecting everything in the plane of the sky, special techniques have to be incorporated to fully understand this structure [4]. The scattering process is critical for interpreting these observations. Coronal
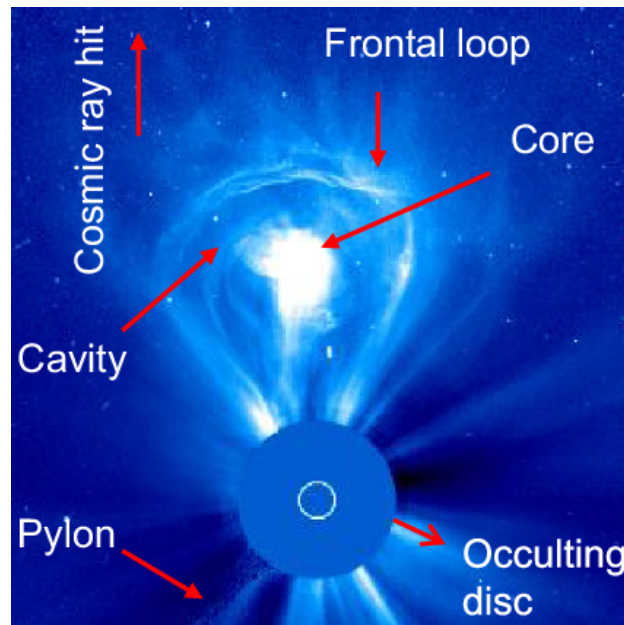

Fig 3: Three-part structure of a CME observed by LASCO/C3 coronagraph, showing the bright front, dark cavity, and bright core.

Mass Ejections (CMEs) are observed in white-light images through Thomson scattering, which is the elastic scattering of solar photospheric light by free electrons in the corona and heliosphere [7, 8]. This scattering process is independent of wavelength and temperature, making white-light observations particularly valuable for studying CMEs [9]. Thomson scattering is valid under specific conditions: the wavelength of the incident light must be much smaller than the average separation between particles in the plasma, and the photon energy must be significantly less than the rest mass energy of the scattering electrons—conditions that are well satisfied for visible sunlight interacting with the coronal plasma. The observed intensity of Thomson-scattered light depends on the geometry between the Sun, the scattering

location, and the observer. The key parameter is the scattering angle (x), defined as the angle between the incident solar beam and the observer's line of sight. When decomposed, the scattered light has two components: one transverse to the incident beam, which is isotropic, and another parallel to it, which varies as the square of the cosine of the scattering angle ($\cos^2 x$). The Thomson surface (TS), defined by x = 90°, represents the geometric surface where the line of sight is perpendicular to the incoming solar radiation. While the scattering efficiency is theoretically lowest at x = 90°, the combined influence of the angular dependence, the distribution of electron density, and the intensity of the incident light leads to the observed brightness peaking along the TS. This makes the TS the effective region for maximum visibility of CMEs at a given radial distance. Observations have also shown that the scattered intensity spreads beyond the TS, forming what is known as the Thomson plateau—an effect more pronounced in unpolarized images [10]. In contrast, polarized brightness is more localized near the TS [11]. Collectively, these factors determine how the brightness and morphology of CMEs appear to observers at different vantage points, and thus play a crucial role in interpreting CME dynamics and structure in heliospheric imaging [4].

1.2.2   In Situ Observations

In-situ spacecraft detect CMEs (ICMEs) by measuring plasma, magnetic field, and compositional changes as the CME passes over the spacecraft. Key signatures include enhanced magnetic fields, smooth field rotation (in Magnetic Clouds), and low plasma beta [12, 13, 14]. Due to their large 3D
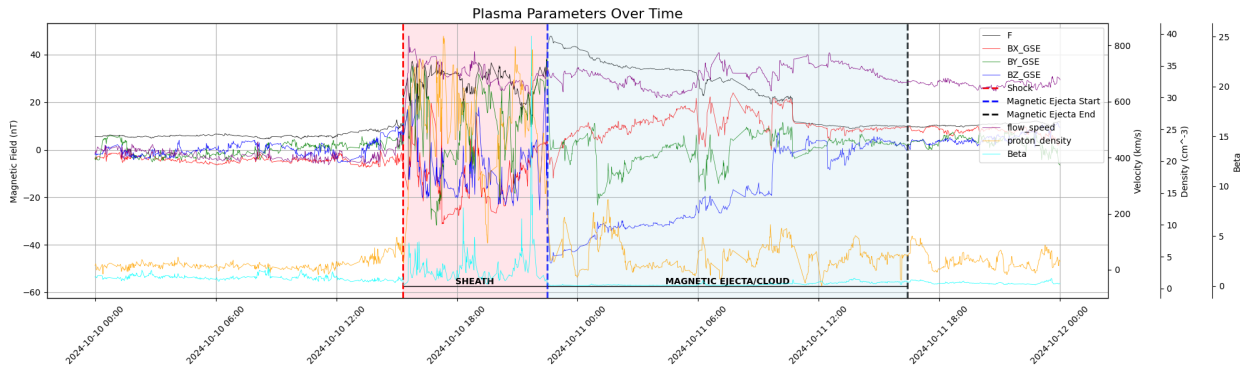
Fig 4: In-situ measurements of an ICME showing characteristic signatures: magnetic field enhancement, rotation, and plasma parameter changes.

structure, ICMEs appear differently depending on the spacecraft's trajectory. Thus, multi-point in-situ observations are crucial for accurate identification and correlation with remote observations [17, 18, 5]. Fast CMEs often drive a forward shock ahead of them, identified in in-situ data by sudden increases in plasma density, temperature, speed, and magnetic field [19]. This shock

is followed by a sheath region—a turbulent and compressed zone of solar wind characterized by strong magnetic field fluctuations and deflections. The sheath can enhance geomagnetic activity, especially when the magnetic field is compressed perpendicular to the shock surface [20, 21]. The magnetic field draping around the ICME within the sheath further contributes to its geoeffectiveness.

2 ICME Signatures and Structures

Interplanetary Coronal Mass Ejections (ICMEs) are the interplanetary manifestations of CMEs, detected through in-situ measurements by spacecraft such as WIND, ACE, and STEREO. These structures are characterized by distinct plasma, magnetic field, and compositional signatures that distinguish them from the ambient solar wind. Understanding these signatures is crucial for identifying ICMEs and assessing their potential space weather impacts. The following sections describe the general signatures of ICMEs and the specific characteristics of flux ropes, a common structural component of ICMEs.

2.1 General ICME Signatures

ICMEs are identified in in-situ data through a combination of plasma, magnetic, and compositional anomalies. Key signatures include:

- **Enhanced Magnetic Field**: ICMEs often exhibit stronger magnetic fields (10-20 nT at 1 AU) compared to the typical solar wind (5-10 nT). This enhancement is due to the compressed and organized magnetic structure within the ICME [25].

- **Low Plasma Beta**: The plasma beta, defined as the ratio of thermal pressure to magnetic pressure, is typically low ($\beta < 1$) in ICMEs, indicating that the magnetic field dominates the dynamics [12].

- **Decreasing Velocity Profile**: Expanding ICMEs show a gradual decrease in speed as the trailing edge moves slower than the leading edge, a signature of their expansion in interplanetary space [26].

- **Low Proton Temperature**: ICMEs often have proton temperatures lower than expected for the solar wind at a given speed ($T_p < 0.5T_{\exp}$), reflecting their expansion and cooling [13].

- **Compositional Anomalies**: ICMEs may show elevated alpha-to-proton ratios, enrichment of heavy ions (e.g., Fe, O), and unusual charge states, such as high Fe charge states (Fe^{16+}) or low charge states from prominence material [15, 16].

- **Bidirectional Electrons**: Bidirectional streaming of suprathermal electrons (*energies* > 80 eV) is a common signature, indicating closed magnetic field lines that connect back to the Sun, often observed in magnetic clouds [27].

2.2 Flux Ropes

A significant subset of ICMEs, known as magnetic clouds, exhibit a distinct magnetic structure called a flux rope. A flux rope is a coherent, helical magnetic field configuration characterized by a strong magnetic field with a smooth rotation in direction over time as the structure passes the spacecraft. The defining features of flux ropes include:

- **Smooth Magnetic Field Rotation**: The magnetic field vector rotates gradually, often over 12-48 hours, indicating a twisted, helical structure. This rotation is typically observed in one or two components of the magnetic field in the spacecraft's reference frame [25].

- **Enhanced Magnetic Field Strength**: The magnetic field within a flux rope is stronger at the center, decreasing toward the edges, consistent with a cylindrical or toroidal geometry [12].

- **Low Plasma Beta**: The plasma beta within flux ropes is typically very low ($\beta \ll 1$), as the magnetic field dominates the pressure, contributing to the structure's stability [26].

- **Geoeffectiveness**: Flux ropes are particularly geoeffective when their magnetic field includes a southward component ($B_z < 0$) in the geocentric solar magnetospheric (GSM) coordinate system, as this orientation facilitates magnetic reconnection with Earth's magnetosphere, potentially triggering geomagnetic storms [1].

Magnetic Cloud Type	SEN	SWN	NES	NWS
Leading Field	South (-Bz)	South (-Bz)	North (+Bz)	North (+Bz)
Axial Field	East (+By)	West (-By)	East (+By)	West (-By)
Trailing Field	North (+Bz)	North (+Bz)	South (-Bz)	South (-Bz)
Helicity	LH	RH	RH	LH

Fig 5: Magnetic field configurations in the ecliptic plane showing typical flux rope orientations.

Flux ropes are thought to originate from the eruption of twisted magnetic structures in the solar corona, such as prominences or active region filaments.

Magnetic Cloud Type	WNE	ESW	ENW	WSE
Leading Field	West (-By)	East (+By)	East (+By)	West (-By)
Axial Field	North (+Bz)	South (-Bz)	North (+Bz)	South (-Bz)
Trailing Field	East (+By)	West (-By)	West (-By)	East (+By)
Helicity	RH	RH	LH	LH

Fig 6: Magnetic field configurations perpendicular to the ecliptic plane showing different flux rope types.

Their helical structure is preserved as they propagate through interplanetary space, although interactions with the solar wind can distort their shape. Models such as the Grad-Shafranov reconstruction or cylindrical force-free models are often used to infer the 3D structure of flux ropes from in-situ data [3]. The presence of a flux rope within an ICME is a strong indicator of its potential to cause significant space weather effects, particularly when associated with a preceding shock and sheath region.

3 Shock Formation and Kinematics

Collisionless shocks, prevalent in interplanetary space and other astrophysical environments, differ fundamentally from collisional shocks observed in ordinary gases. In a collisional shock, molecular collisions facilitate momentum and energy transfer, leading to a thin shock front on the order of a few mean free paths. In contrast, collisionless shocks in space plasmas, such as those driven by coronal mass ejections (CMEs), occur in environments where the mean free path is vast—often exceeding 1 AU in the solar wind, compared to shock thicknesses of 100-1,000 km [2]. This absence of collisions necessitates alternative mechanisms for dissipation and plasma heating, involving complex interactions between particles and electromagnetic fields. Understanding these mechanisms is critical because collisionless shocks are ubiquitous in space, from planetary bow shocks to interplanetary shocks driven by fast CMEs, and they significantly influence space weather by accelerating particles, compressing magnetic fields, and triggering geomagnetic disturbances. The shock standoff distance, the separation between the shock front and the driving CME, is a key parameter that quantifies the shock's geometry and its interaction with the ambient medium, directly impacting its geoeffectiveness. Studying the formation and standoff distance of these shocks enhances our ability to predict their effects on Earth's magnetosphere and space-based infrastructure. Fast-moving CMEs in interplanetary space drive shocks when their speed exceeds the local magnetosonic speed of the ambient solar wind, typically 400-600 km/s at 1 AU. These shocks form due to the steepening of large-amplitude magnetohydrodynamic (MHD) waves, particularly the fast-mode wave, which propagates faster than the Alfvén and slow modes in a magnetized plasma [2]. The steepening process occurs because the wave speed depends on the plasma's local density and magnetic field strength, which the wave itself modifies. As a fast-mode wave propagates, regions of higher density or stronger magnetic fields travel faster, causing the wave front to steepen and form a sharp discontinuity—a shock. This shock is characterized by abrupt changes in plasma density, temperature, velocity, and magnetic field strength, governed by the Rankine-Hugoniot relations, which ensure conservation of mass, momentum, and energy across the shock front [22]. Unlike collisional shocks, where viscosity and friction provide dissipation, collisionless shocks rely on field-particle interactions, such as ion reflection and wave-particle scattering, to dissipate energy. This results in a complex shock structure with features like a foot, ramp, and overshoot, as observed in the Earth's bow shock [2]. The shock standoff distance, defined as the distance between the shock front and the leading edge of the CME (the driver), is a critical parameter for understanding the shock's kinematics and its interaction with the solar wind. This distance is determined by the
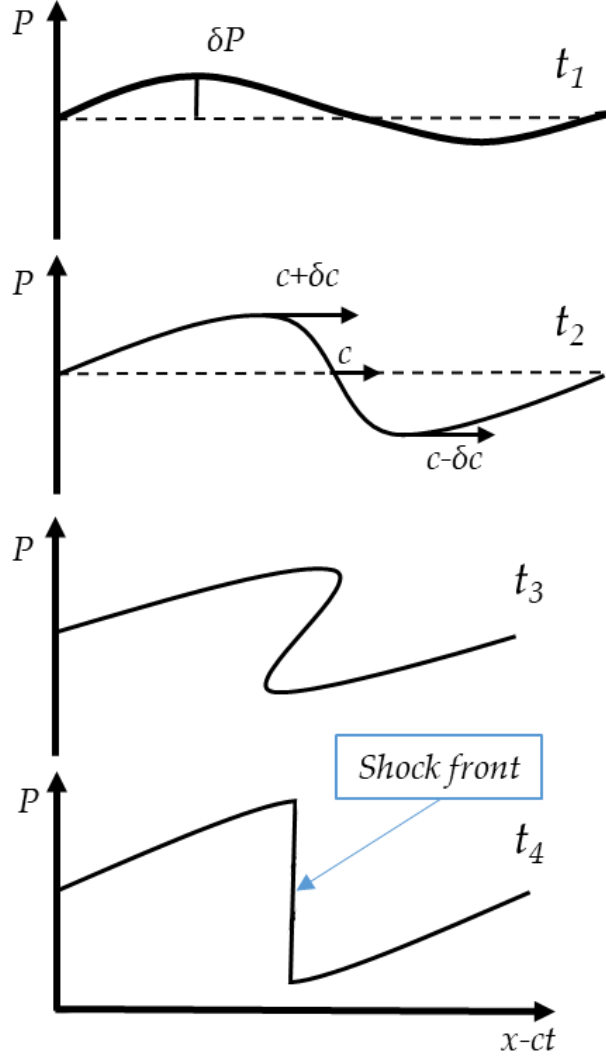
Fig 7: Wave steepening process leading to shock formation, showing the evolution of plasma parameters.

balance between the dynamic pressure of the CME and the resisting pressure of the ambient medium. In a collisionless plasma, the standoff distance is influenced by the CME's speed, the density ratio between the solar wind and the CME, and the magnetic field strength. A simplified gas-dynamic model, adapted from planetary bow shocks, approximates the standoff distance Δ as:

$$\Delta \propto \frac{R_{\mathrm{CME}}}{\rho_{\mathrm{sw}}/\rho_{\mathrm{CME}}}$$

where R_{CME} is the radius of curvature of the CME's leading edge, ρ_{sw} is the solar wind density, and ρ_{CME} is the CME density [23]. A higher density ratio results in a smaller standoff distance due to increased compression, while a stronger CME magnetic field can push the shock further ahead by resisting compression. Observations at 1 AU, such as those from WIND and ACE, indicate standoff distances typically range from 0.05 to 0.2 AU for fast CMEs

[24, 6]. The standoff distance is crucial because it determines the size of the sheath region—the turbulent, compressed zone of solar wind between the shock and the CME—which enhances geomagnetic activity when it contains southward magnetic fields [1]. Understanding the standoff distance allows us to model the shock's geometry and predict its impact on Earth's magnetosphere, aiding in space weather forecasting.

3.1 Parameters Influencing Shock Standoff Distance

Several key parameters influence the shock standoff distance:

- **CME Speed**: Faster CMEs generate stronger shocks with larger standoff distances due to increased dynamic pressure. The relative speed between the CME and the solar wind ($v_{\mathrm{CME}} - v_{\mathrm{sw}}$) determines the Mach number, which directly affects the shock strength and standoff distance [2].

- **Solar Wind Density**: A denser solar wind increases compression at the shock front, reducing the standoff distance. Typical solar wind density at 1 AU is 5-10 cm^{-3}, but variations during solar activity significantly alter this parameter.

- **Magnetic Field Strength**: The magnetic field within the CME and solar wind affects the Alfvén and magnetosonic speeds, influencing shock formation and standoff distance. Stronger CME magnetic fields lead to larger standoff distances due to increased magnetic pressure [24].

- **CME Geometry**: The curvature and size of the CME's leading edge affect the shock's geometry. A larger radius of curvature results in a larger standoff distance, as the shock forms further ahead of the CME [23].

These parameters are studied using both remote sensing (e.g., LASCO, STEREO) and in-situ observations (e.g., WIND, ACE), which provide complementary data to model the shock's evolution and its interaction with the interplanetary medium [5].

4 Analysis of Sudden Storm Commencements and Shock Standoff Distance

This study focuses on analyzing the relationship between Sudden Storm Commencements (SSCs) observed on Earth and the shock standoff distance of Interplanetary Coronal Mass Ejections (ICMEs) detected at the L1 point. SSCs are abrupt increases in the geomagnetic field, often associated with the arrival of interplanetary shocks driven by fast CMEs. The goal is to investigate whether the shock standoff distance, the distance between the shock front and the CME's leading edge, correlates with the strength of SSCs, which could enhance our understanding of their geoeffectiveness.

4.1 Methodology

The analysis began with the Dst index data from the World Data Center for Geomagnetism, Kyoto (`https://wdc.kugi.kyoto-u.ac.jp/wdc/Sec3.html`), which provides measurements of the Disturbance Storm Time (Dst) index, a proxy for geomagnetic activity. The Dst index was used to identify the strongest SSC events, characterized by significant negative excursions in Dst, indicating intense geomagnetic disturbances. A filtering methodology was applied to select the top 20 SSC events based on the magnitude of the Dst decrease. The dates of these events were recorded and are listed in Table 2. These SSC event dates were cross-referenced with in-situ data from the Coordinated Data Analysis Web (CDAWeb) at `https://cdaweb.gsfc.nasa.gov/`, managed by NASA's Goddard Space Flight Center, which provides access to data from solar physics instruments, including WIND and ACE spacecraft at the L1 point. The in-situ data included measurements of magnetic field strength, plasma density, velocity components, proton temperature, and ion ratios (e.g., alpha-to-proton ratio). For each SSC event date, the corresponding in-situ data were analyzed to identify ICME signatures, such as enhanced magnetic fields, low plasma beta, and shock-sheath structures (as discussed in Section 2.1). Shocks were identified by sudden jumps in velocity, density, temperature, and magnetic field strength, while the leading edge of the magnetic ejecta was marked by a significant increase in magnetic field strength, often associated with a flux rope or magnetic cloud. To estimate the shock standoff distance, the time difference between the shock arrival and the leading edge arrival of the magnetic ejecta was determined from the in-situ data. The basic standoff distance was computed by integrating the plasma bulk velocity over this time interval:

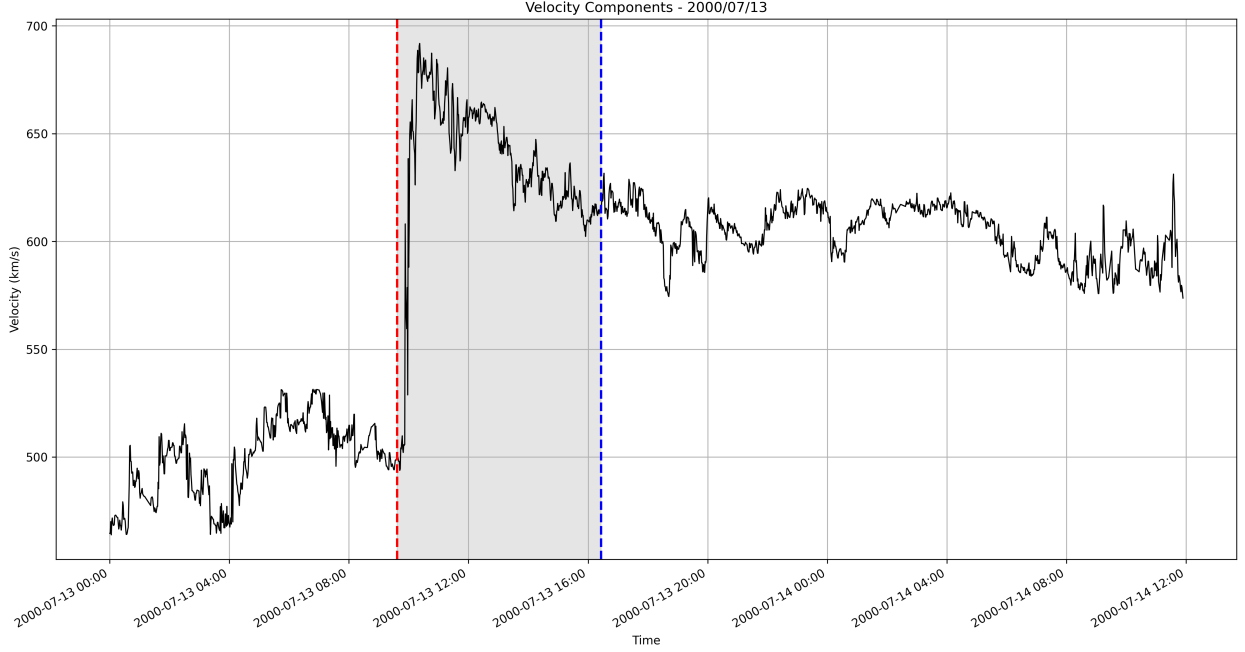$$D = \int_{t_{\text{shock}}}^{t_{\text{leading}}} v(t)\,dt,$$

Fig 8: In-situ plasma velocity profile showing shock arrival and CME passage with expansion characteristics.

where $v(t)$ is the measured bulk flow speed between the shock arrival time t_{shock} and the leading edge time t_{leading}. This integral represents the distance the spacecraft traverses through the sheath structure, under the assumption of no internal expansion or contraction within the sheath. However, in reality, CMEs often undergo self-similar expansion or contraction as they propagate through interplanetary space. Even in the absence of bulk acceleration, such internal evolution is reflected in the velocity profile. A monotonic decrease in velocity from the shock front to the leading edge indicates expansion, while a monotonic increase indicates contraction. To account for this, an expansion (or contraction) velocity V_{exp} can be estimated as:

$$V_{\text{exp}} = \frac{1}{2}(v_{\text{shock}} - v_{\text{leading}}),$$

where v_{shock} and v_{leading} are the velocities at the times of shock arrival and leading edge, respectively. The total contribution of this expansion (or contraction) to the observed distance is given by:

$$\Delta D = V_{\text{exp}} \cdot (t_{\text{leading}} - t_{\text{shock}}).$$

Depending on the physical interpretation point (shock arrival or sheath end) and the nature of the CME evolution (expansion or contraction), this correction is applied to adjust our calculation for standoff distance as follows:

- **If the CME is expanding:**

13

– To estimate the standoff distance at the *shock arrival* time, subtract the correction:

$$D_{\text{shock}} = \int_{t_{\text{shock}}}^{t_{\text{leading}}} v(t)\,dt - \Delta D$$

– To estimate the standoff distance at the *sheath end* time, add the correction:

$$D_{\text{trailing}} = \int_{t_{\text{shock}}}^{t_{\text{leading}}} v(t)\,dt + \Delta D$$

- **If the CME is contracting:**

  – To estimate the standoff distance at the *shock arrival* time, add the correction:

$$D_{\text{shock}} = \int_{t_{\text{shock}}}^{t_{\text{leading}}} v(t)\,dt + \Delta D$$

  – To estimate the standoff distance at the *sheath end* time, subtract the correction:

$$D_{\text{trailing}} = \int_{t_{\text{shock}}}^{t_{\text{leading}}} v(t)\,dt - \Delta D$$

The integral was approximated using the trapezoidal rule, a numerical integration method that estimates the area under the velocity-time curve by dividing the interval into subintervals and approximating each as a trapezoid. For discrete data points (t_i, v_i), the trapezoidal rule is applied as follows: the method takes the first two data points (t_1, v_1) and (t_2, v_2) to calculate the area of the first trapezoid as $\frac{(v_1+v_2)}{2}(t_2 - t_1)$, then proceeds to the next pair (t_2, v_2) and (t_3, v_3), calculating the area as $\frac{(v_2+v_3)}{2}(t_3 - t_2)$, and so on for each consecutive pair of data points. The total area is the sum of these trapezoidal areas:

$$D \approx \sum_{i=1}^{n-1} \frac{(v_i + v_{i+1})}{2}(t_{i+1} - t_i).$$

This method provides an accurate approximation when the velocity profile is sampled at sufficient resolution. This framework allows for a more accurate determination of the physical standoff distance at L1, accounting for the evolving nature of the CME structure.

Table 1: Calculated Standoff Distance (in Solar Radii) of few Strong CMEs. The second column represents the distance traveled by the spacecraft (WIND) through the sheath, approximated via the trapezoidal rule. The third and fourth columns represent the calculated standoff distances at the shock arrival and at the sheath end, respectively.

Date	Distance travelled by WIND	Calculated SOD (At Shock)	Calculated SOD (At Sheath End)	Flux Type
2024-10-10	25.9	25.7	26.2	WSE
2005-05-14	12.7	9.59	15.8	ENW
2005-09-10	–	–	–	-
2004-12-04	–	–3	–	-
2024-05-10	64.6	53.8	75.3	SEN
2004-01-24	2.7	2.6	2.8	-
2022-03-13	28.7	28.0	29.4	ENW
2012-03-08	60.4	59.4	61.5	WSE
2015-06-22	25.3	23.4	27.1	SEN
2015-03-17	20.6	18.0	23.2	WSE
2017-08-31	–	–	–	-
2004-11-09	42.4	39.1	45.8	WSE
2001-04-11	31.4	28.5	34.3	Difficult to say
2002-05-23	–	–	–	-
2001-11-23	15.7	15.4	16.0	SWN
2003-11-20	13.3	12.6	14.0	ESW

Table 1: Calculated Standoff Distance (in Solar Radii) of few Strong CMEs. The second column represents the distance traveled by the spacecraft (WIND) through the sheath, approximated via the trapezoidal rule. The third and fourth columns represent the calculated standoff distances at the shock arrival and at the sheath end, respectively.

Date	Distance travelled by WIND	Calculated SOD (At Shock)	Calculated SOD (At Sheath End)	Flux Type
2002-11-20	–	–	–	-
2001-10-21	25.1	19.6	30.5	WNE
2002-09-07	32.3	29.5	35.1	SEN
2002-09-30	26.2	25.3	27.1	NES
1998-05-03	35.2	33.9	36.6	ENW
2001-03-30	16.7	15.3	18.2	Difficult to say
2000-04-06	46.4	47.0	47.5	SWN
1998-09-24	35.7	32.1	39.2	ESW
2000-07-13	22.5	21.7	23.4	NWS
2000-09-17	27.9	24.2	31.7	ENW
2000-08-11	35.0	32.1	37.9	SEN

We tried analyzing a number of CMEs, drawing from the catalog by Richardson and Cane [18], and attempted to obtain their Stand-Off Distances (SOD) using our model. Table 1 summarizes the plasma parameters, providing insights into the standoff distances calculated at different points (Trapezoidal, At Shock, and At Sheath End) along with the associated flux types where available. In this methodology, we analyzed the area under the curve corresponding to each CME event and applied necessary corrections to account for the expansion or contraction of the CME, which may arise due to various physical phenomena. Using this corrected approach, we estimated the standoff distance both at the shock arrival time and at the sheath

end time. A total of around twenty seven such events were studied, and based on this analysis, we further compared the events by examining key shock parameters such as the compression ratio, ram pressure, and shock speed. Our goal was to investigate whether any consistent correlations exist among these parameters. The values obtained through this process have been systematically tabulated and are presented in the table above. However, it is important to note that the sample size is relatively small, and our interpretations are made with this limitation in consideration. Finally, a statistical analysis was performed to explore any correlation between the shock standoff distance and the SSC strength, as measured by the Dst index. This involved comparing the standoff distances for the selected events with the corresponding Dst values to identify potential trends or dependencies.

4.2   Findings

The objective of this analysis was to investigate whether the strongest interplanetary shocks—potentially associated with fast ICMEs—correlate with the most intense SSC events, as indicated by large negative Dst values. To explore this, we attempted to estimate shock standoff distances at L1 using in-situ solar wind and magnetic field measurements from WIND and ACE spacecraft. However, while some events did exhibit clear shock signatures—such as sudden jumps in plasma parameters (density, temperature, speed) and magnetic field strength—the overall dataset was insufficient to draw firm conclusions. Despite these findings, a definitive correlation between shock strength (as inferred from standoff distance or velocity jumps) and the intensity of SSCs could not be established. The primary limitation was the small sample size, which stemmed either from a lack of reliable in-situ data, the absence of well-defined ICME structures during key periods, or gaps in observational coverage. Consequently, this analysis remains inconclusive. A significantly larger event set—combined with careful identification of ICME-driven shocks and improved standoff distance estimation—is essential to determine whether a meaningful relationship exists between shock geometry and geomagnetic storm strength. This work highlights the need for a more comprehensive analysis, including a larger dataset and detailed examination of plasma parameters (e.g., density, temperature, magnetic field strength) to better understand the relationship between shock standoff distance and SSC strength.

Date (UTC)	Delta Peak(nT)	ICME (Y/N)	Shock (Y/N)	Shock Spd (km/s)	Flux type	SOD (Rs)	n2/n1	Us (km/s)	Mach (M)	Ramp1 (nPa)	Ramp2 (nPa)
2012-06-16 22:00	-77.0	Y	Y	489.32	–	–	2.06	489.3	7.78	4.30e-9	1.05e-8
2024-08-11 19:00	-71.0	Y	N	–	–	–	–	–	–	–	–
2004-12-05 08:00	-67.0	N	N	–	–	–	–	–	–	–	–
2024-05-10 17:00	-66.0	Y	Y	701.85	–	–	2.10	701.8	13.28	5.55e-9	1.96e-8
1999-04-16 15:00	-65.0	Y	Y	477.4	–	–	1.66	–	5.03	1.67e-9	1.67e-9
2002-05-23 11:00	-63.0	Y	Y	559.63	–	–	1.50	–	4.13	1.67e-9	1.67e-9
2004-11-07 19:00	-61.0	Y	Y	651.68	WSE	–	2.32	651.7	3.27	5.17e-9	1.75e-8
2017-08-31 06:00	-60.0	N	N	–	–	–	–	–	–	–	–
2002-03-18 15:00	-59.0	Y	N	–	–	–	–	–	–	–	–
2025-03-21 16:00	-58.0	N	N	–	–	–	–	–	–	–	–
2012-01-22 07:00	-57.0	Y	N	–	–	–	–	–	–	–	–
2001-12-29 06:00	-55.0	Y	N	–	–	–	–	–	–	–	–
2005-05-15 03:00	-52.0	Y	Y	check	ENW	–	1.37	–	–	–	–
2000-07-13 10:00	-51.0	Y	Y	651.22	NWS	21.7	3.29	–	6.00	1.67e-9	1.67e-9
2011-02-18 04:00	-51.0	Y	Y	463.29	–	–	4.12	–	8.70	1.67e-9	1.67e-9
2000-07-11 05:00	-50.0	Y	N	–	–	–	–	–	–	–	–
1997-01-11 01:00	-50.0	Y	N	–	–	–	–	–	–	–	–
2024-08-17 18:00	-48.0	Y	N	–	–	–	–	–	–	–	–
1999-05-18 03:00	-48.0	Y	N	–	–	–	–	–	–	–	–
2024-10-10 15:00	-47.0	Y	Y	828.41	–	–	3.79	4.24	–	1.67e-9	1.67e-9
2016-08-02 14:00	-47.0	Y	Y	–	–	–	3.79	–	–	1.67e-9	1.67e-9
2000-01-27 16:00	-47.0	–	–	–	–	–	3.79	–	–	1.67e-9	1.67e-9
2016-07-20 15:00	-46.0	Y	Y	432.06.41	–	–	3.79	–	9.60	1.67e-9	1.67e-9

Column Descriptions:

- **Date (UTC)**: Timestamp of Dst peak

- **Delta Peak (nT)**: SSC Peak's

- **ICME (Y/N)**: Coronal Mass Ejection presence

- **Shock (Y/N)**: Shock Present

- **Shock Spd (km/s)**: Shock speed

- **Flux**: Solar wind flux type

- **SOD (Rs)**: Stand-Off Distance in Solar radii

- **n2/n1**: Density ratio across shock

- **Us (km/s)**: Shock speed $(n_2 V_2 - n_1 V_1)/(n_2 - n_1)$

- **Mach (M)**: Mach number V_1/V_f

- **Ramp1/2 (nPa)**: Ram pressure $0.5 n V^2$

Table 2: SSC Dst Peaks with Solar Wind Shock Parameters

5 Conclusion and Future Work

This study presents an effort to understand the dynamics of Coronal Mass Ejections (CMEs) and their interplanetary counterparts (ICMEs) as they propagate through space, with a particular focus on identifying and analyzing the shock standoff distances associated with these structures. The investigation began with an attempt to interpret CME morphology through both remote sensing observations and in-situ spacecraft measurements. By examining various in-situ signatures — such as time profiles of velocity, magnetic field, and plasma parameters — we identified distinct regions within ICMEs, including the shock front, the sheath region, and the magnetic flux rope structure. These identifications were crucial for calculating key shock-related parameters, including the standoff distance. A significant part of the analysis was devoted to understanding how CME expansion or contraction — as observed in velocity profiles — influences our calculations of the standoff distance. We developed a methodology that allowed for corrections due to expansion or contraction and estimated the standoff distance both at the moment of shock arrival and at the sheath end. This was carried out for approximately twenty seven events, and we attempted to examine correlations between standoff distances and other shock parameters such as compression ratio, ram pressure, and shock speed. These results, although indicative, are constrained by the limited sample size and gaps in data quality. Moreover, this work does not include a rigorous uncertainty or error analysis, which remains a limitation. Nonetheless, the study has provided valuable insights into how interplanetary shocks and their associated parameters manifest in observational data and how they may relate to space weather effects at Earth, such as Sudden Storm Commencements (SSCs). Future work will expand on this analysis by:

- Increasing the sample size of SSC events and corresponding ICME observations to improve statistical significance.

- Analyzing plasma parameters (e.g., plasma density, proton temperature, magnetic field strength, and ion composition) to better understand their role in determining shock standoff distance and SSC strength.

- Incorporating a non linear expansion velocity model to account for CME acceleration, refining the standoff distance calculations.

- Understanding the correlation of Standoff Distance with CME size, compression ratio, etc.

These efforts will improve our ability to predict the geoeffectiveness of CMEs and mitigate their impacts on space-based infrastructure and Earth's magnetosphere.

References

[1] Tsurutani, B. T., et al. (1988). Strong Geomagnetic Storms Caused by ICMEs. *Journal of Geophysical Research*, 93(A8), 8519.

[2] Burgess, D. (2005). Collisionless Shocks. In *Lecture Notes in Physics: The Solar System and Beyond*, 129-148.

[3] Lepping, R. P., et al. (2006). A Summary of WIND Magnetic Clouds for Years 1995-2003: Model-Fitted Parameters, Associated Errors, and Classifications. *Annales Geophysicae*, 24, 215.

[4] Webb, D. F., & Howard, T. A. (2012). Coronal Mass Ejections: Observations. *Living Reviews in Solar Physics*, 9, 3.

[5] Mishra, W. (2017). Propagation of Coronal Mass Ejections from Sun to Earth. *Journal of Astrophysics and Astronomy*, 38, 1.

[6] Temmer, M., et al. (2011). Deriving CME Density from Remote Sensing Data and Comparison to In Situ Measurements. *Astrophysical Journal*, 736, 76.

[7] Billings, D. E. (1966). *A Guide to the Solar Corona*. Academic Press.

[8] Vourlidas, A., & Howard, R. A. (2006). The Proper Treatment of Coronal Mass Ejection Observations. *Astrophysical Journal*, 642, 1216.

[9] Hundhausen, A. J. (1993). Sizes and Locations of Coronal Mass Ejections: SMM Observations from 1980 and 1984-1989. *Journal of Geophysical Research*, 98(A8), 13177.

[10] Howard, T. A., & DeForest, C. E. (2012). The Thomson Surface and CME Visibility in Heliospheric Imaging. *Astrophysical Journal*, 752, 130.

[11] Howard, T. A., et al. (2013). Polarimetric Observations of CMEs with STEREO. *Solar Physics*, 285, 287.

[12] Lepping, R. P., et al. (1990). Magnetic Field Structure of Interplanetary Magnetic Clouds at 1 AU. *Journal of Geophysical Research*, 95(A8), 11957.

[13] Richardson, I. G., & Cane, H. V. (1995). The Identification of Interplanetary Coronal Mass Ejections. *Journal of Geophysical Research*, 100(A12), 23397.

[14] Richardson, I. G., & Cane, H. V. (1997). Sources of Geomagnetic Activity During Nearly Three Solar Cycles. *Journal of Geophysical Research*, 102(A10), 22291.

[15] Zurbuchen, T. H., et al. (2003). Composition of Coronal Mass Ejections. *Astrophysical Journal*, 598, 1410.

[16] Lepri, S. T., & Zurbuchen, T. H. (2010). Iron Charge State Distributions in ICMEs. *Journal of Geophysical Research*, 115, A01112.

[17] Gopalswamy, N. (2006). Coronal Mass Ejections and Their Space Weather Effects. *Space Science Reviews*, 124, 145.

[18] Richardson, I. G., & Cane, H. V. (2010). Near-Earth Interplanetary Coronal Mass Ejections Since January 1996. *Solar Physics*, 264, 189.

[19] Richardson, I. G., & Cane, H. V. (1993). Signatures of Shock Drivers in the Solar Wind. *Journal of Geophysical Research*, 98(A9), 15295.

[20] McComas, D. J., et al. (1989). The Structure of Interplanetary Shocks. *Journal of Geophysical Research*, 94(A11), 14655.

[21] Jurac, S., et al. (2002). Sheath Regions of Interplanetary Coronal Mass Ejections. *Journal of Geophysical Research*, 107(A10), 1286.

[22] Priest, E. R. (1982). *Solar Magnetohydrodynamics*. D. Reidel Publishing Company.

[23] Spreiter, J. R., et al. (1966). Hydromagnetic Flow Around Blunt Bodies. *AIAA Journal*, 4(8), 1398.

[24] Russell, C. T., & Mulligan, T. (2002). The Standoff Distance of Interplanetary Shocks. *Planetary and Space Science*, 50, 527.

[25] Burlaga, L. F., et al. (1981). Magnetic Loop Behind an Interplanetary Shock: Voyager, Helios, and IMP 8 Observations. *Journal of Geophysical Research*, 86(A8), 6673.

[26] Klein, L. W., & Burlaga, L. F. (1982). Interplanetary Magnetic Clouds at 1 AU. *Journal of Geophysical Research*, 87(A2), 613.

[27] Gosling, J. T., et al. (1987). Bidirectional Solar Wind Electron Heat Flux Events. *Journal of Geophysical Research*, 92(A8), 8519.